Blind Image Deblurring Using Dark Channel Prior
Supplemental Material

Jinshan Pan[1,2,3] Deqing Sun[3,4] Hanspeter Pfister[3] Ming-Hsuan Yang[2]
[1]Dalian University of Technology [2]UC Merced [3]Harvard University [4]NVIDIA

Overview

In this supplemental material, we provide the proofs of **Property 1** and **Property 2** in Sections 1 and 2 respectively. We analyze the properties of the dark channel prior in image deblurring and demonstrate its effectiveness on natural images, text images and low-illumination images in Section 3. Section 4 provides detailed analysis of the proposed algorithm The algorithm details for solving (10) in the manuscript and the proposed non-uniform deblurring algorithm are presented in Sections 5 and 6, respectively. We qualitatively evaluate the proposed method and compare it against existing deblurring methods on the publicly available datasets by Köhler *et al*. [10], Levin *et al*. [13], and Sun *et al*. [18] in Section 7. Finally, we show more visual comparisons in Section 8.

1. Proof of Property 1

Property 1: *Let $D(B)$ and $D(I)$ denote the dark channel of the blurred and clear images, we have:*

$$D(B)(\mathrm{x}) \geq D(I)(\mathrm{x}). \tag{1}$$

Proof: Let Ω_k and s denote the domain and size of the blur kernel k. Based on the definition of convolution, we have:

$$B(\mathrm{x}) = \sum_{\mathrm{z}\in\Omega_k} I(\mathrm{x} + \left[\frac{\mathrm{s}}{2}\right] - \mathrm{z})k(\mathrm{z}). \tag{2}$$

According to the definition of dark channel,

$$\begin{aligned}
D(B)(\mathrm{x}) &= \min_{\mathrm{y}\in\mathcal{N}(\mathrm{x})} B(\mathrm{y}) \\
&= \min_{\mathrm{y}\in\mathcal{N}(\mathrm{x})} \sum_{\mathrm{z}\in\Omega_k} I(\mathrm{y} + \left[\frac{\mathrm{s}}{2}\right] - \mathrm{z})k(\mathrm{z}) \\
&\geq \sum_{\mathrm{z}\in\Omega_k} \min_{\mathrm{y}\in\mathcal{N}(\mathrm{x})} I(\mathrm{y} + \left[\frac{\mathrm{s}}{2}\right] - \mathrm{z})k(\mathrm{z}) \\
&\geq \sum_{\mathrm{z}\in\Omega_k} \min_{\mathrm{y}\in\mathcal{N}^{\mathcal{I}}(\mathrm{x})} I(\mathrm{y})k(\mathrm{z}) \\
&= \sum_{\mathrm{z}\in\Omega_k} D(I)(\mathrm{x})k(\mathrm{z}) \\
&= D(I)(\mathrm{x}).
\end{aligned}$$

□

To make the consistency of coordinates in $D(B)$ and $D(I)$, we use larger image patch $\mathcal{N}^{\mathcal{I}}(\mathrm{x})$. Let $\mathcal{S}_{\mathcal{N}}$, $\mathcal{S}_{\mathcal{N}^{\mathcal{I}}}$, and $\mathcal{S}_k$ denote the size of image patches $\mathcal{N}(\mathrm{x})$, $\mathcal{N}^{\mathcal{I}}(\mathrm{x})$, and blur kernel k. It satisfies: $\mathcal{S}_{\mathcal{N}^{\mathcal{I}}} = \mathcal{S}_{\mathcal{N}} + \mathcal{S}_k$. If we use the same image patch size for the both the clear and the blurred images, the inequality roughly holds, but **Property 2** still holds at this case.

2. Proof of Property 2

Intuitively the blur process removes zero elements in the clear image. Therefore the blurred images have fewer zero-intensity pixels, or equivalently, less sparse dark channels, than the clear images.

Property 2: *Let Ω denote the domain of an image I. If there exist some pixels $\mathrm{x} \in \Omega$ such that $I(\mathrm{x}) = 0$, we have:*

$$\|D(B)(\mathrm{x})\|_0 > \|D(I)(\mathrm{x})\|_0, \tag{3}$$

Proof: In this proof, we exclude the trivial case that the clear image has only zero-intensity pixels.

Property 1 demonstrates that the value of $D(B)(\mathrm{x})$ is larger than that of $D(I)(\mathrm{x})$. As the L_0 norm $\|D(B)(\mathrm{x})\|_0$ counts the number of non-zero elements of $D(B)$, we can directly obtain $\|D(B)(\mathrm{x})\|_0 > \|D(I)(\mathrm{x})\|_0$.

In the following, we discuss the validity of **Property 2** when we use the same patch size to compute the dark channels in the clear and blurred images, *i.e.* $\mathcal{S}_{\mathcal{N}^{\mathcal{I}}} = \mathcal{S}_{\mathcal{N}}$. Consider a zero-intensity pixel x in the clear image, *i.e.* $I(\mathrm{x}) = 0$. Let $\mathcal{N}(\mathrm{x})$ denote the patch centered at the pixel x with size the same as the blur kernel. We have $D(I)(\mathrm{x}) = I(\mathrm{x}) = 0$.

Now we will show that the corresponding pixel in the blurred image becomes non-zero under very mild conditions. We can find a pixel $\mathrm{z}' \in \Omega_k$ that satisfies: $k(\mathrm{z}') \neq 0$ and $I(\mathrm{x} + \left[\frac{\mathrm{s}}{2}\right] - \mathrm{z}') \neq 0$. Thus, we have

$$\begin{aligned} B(\mathrm{x}) &= \sum_{\mathrm{z} \in \Omega_k} I(\mathrm{x} + \left[\frac{\mathrm{s}}{2}\right] - \mathrm{z}) k(\mathrm{z}) \\ &\geq I(\mathrm{x} + \left[\frac{\mathrm{s}}{2}\right] - \mathrm{z}') k(\mathrm{z}') > 0. \end{aligned} \tag{4}$$

Note that it is rare to have large regions with all zero pixels. Even for such regions, the clear and blurred images should have the same number of zero dark channel pixels within the region. Moreover, across the boundaries between the all-zero regions and other normal regions, the inequality (4) still holds. As the zero (dark) pixels are removed by the blur process, the dark channel of the blurred image is less sparse than that of the clear image, *i.e.* $\|D(B)(\mathrm{x})\|_0 > \|D(I)(\mathrm{x})\|_0$. □

Remark 1: When the blur kernel is a delta kernel, we always have $B(\mathrm{x}) = I(\mathrm{x})$. Since the goal of our work is to remove blur effect from blurred images, we do not consider this extreme case.

Remark 2: Another explanation for **Property 2** is as follows: for a non-delta blur kernel, if $B(\mathrm{x}) = 0$, there should be more than one zero pixels in the neighborhood of x in the clear image I. However, if $I(\mathrm{x}) = 0$, it is not necessarily true that there exists a pixel y in the neighborhood of x in the blurred image B such that $B(\mathrm{y}) = 0$.

3. Properties of the Dark Channel Prior in Image Deblurring

The dark channel prior is a kind of statistics of the haze-free outdoor images in image dehazing [7]. In image dehazing [7], He *et al*. assume that all the elements of dark channel are zeros. In our work we observe that the blur process reduces the zero elements in the dark channel of the blurred image. As a result the dark channel of clear image contains more zero-intensity values than those of blurred images. Thus, we use L_0-norm on the dark channel to model the sparse property rather than enforce all elements of dark channels to be zero [7]. Our analysis (**Proposition 1** and **Property 2**) indicates that the proposed L_0-regularized dark channel is feasible to image deblurring. Thus, our proposed prior is not limited to outdoor images. It also holds for some specific images, *e.g.*, text images and saturated images. Figure 1(a) and (b) show the sparseness of the dark channel of clear text and saturated images.

In the literature, the normalized sparsity prior [11] also favors clear natural images over blurred ones. However, this property does not always hold for text images and saturated images. As shown in Figure 1 (c) and (d), The normalized sparsity prior may favor the blurred text and low-illumination images over the clear ones.

3.1. Effectiveness of the Dark Channel Prior in Image Deblurring

In the manuscript, we extensively validate the effectiveness of the dark channel prior in image deblurring by using two benchmark datasets [13] and [10]. The results are shown in Figure 2 (*i.e.*, Figure 13 in the manuscript). In this supplemental material, we further evaluate the proposed method using more examples, including natural, text, low-illumination, and face images.

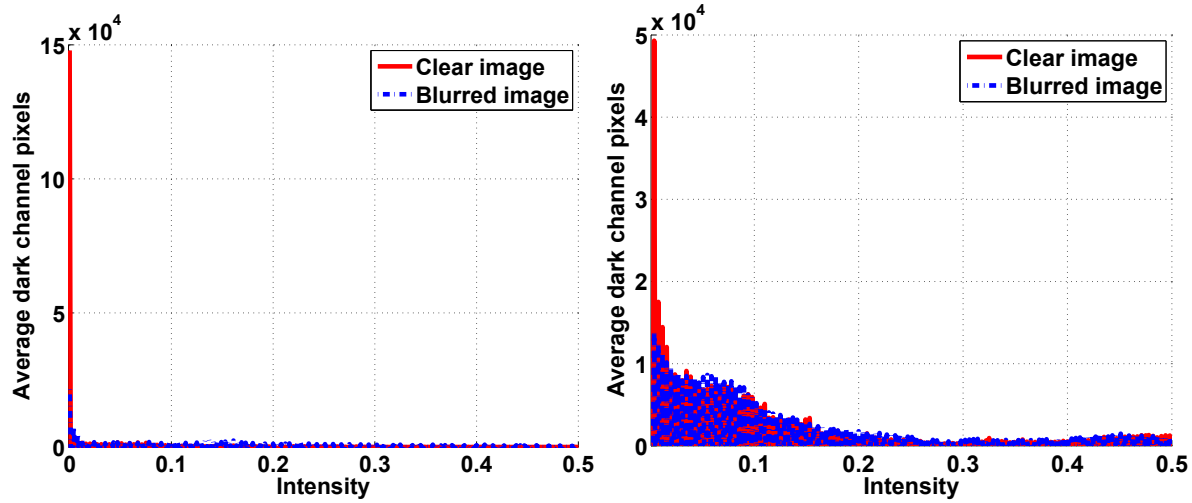

(a) Dark channel on text image dataset [15]

(b) Dark channel on low-illumination image dataset [9]

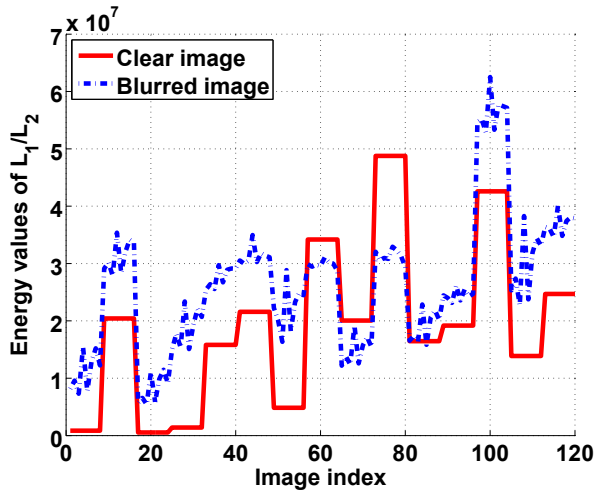

(c) Normalized sparsity prior on text image dataset [15]

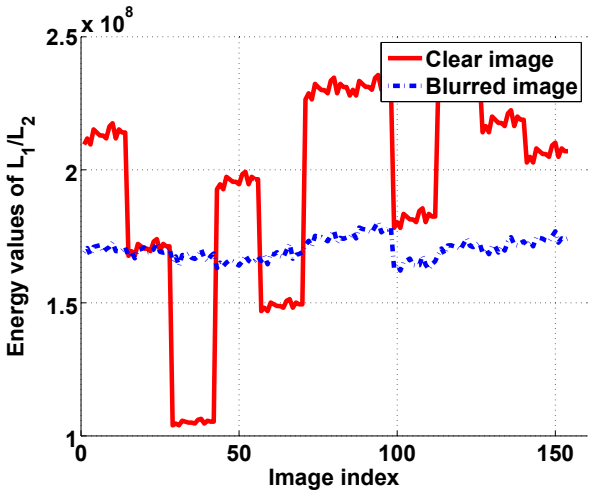

(d) Normalized sparsity prior on low-illumination image dataset [9]

Figure 1. Statistics of the dark channel and normalized sparsity [11] priors on *text* (top) and *low-illumination* (bottom) images. The statistics confirm our analysis that the proposed dark channel prior favors clear images over blurred ones. However, the property does not hold for the normalized sparsity prior [11] on text and low-illumination images.

4. Further Analysis on the Proposed Method

4.1. Convergence Property

We use image gradients (*i.e.*, (16) in the manuscript) to estimate blur kernels, because kernel estimation methods based on gradients have been shown to be more accurate. Therefore we analyze the convergence using the image gradients in the manuscript. In this supplemental material, we further test the convergence property of using image intensity (*i.e.*, (9) in the manuscript) in blur kernel estimation. As shown in Figure 8, using the image intensity also converges.

However, using the image intensity converges to local minima with higher energy than the gradients, suggesting multiple local minima of the proposed objective function. Future work will further investigate the optimization method to avoid poor local minima.

4.2. Computational Complexity and Running Time

Compared to the L_0-regularized methods [15, 23], our method additionally requires computing the dark channel and look-up table. The complexity of this step is $O(N)$ and independent of patch size [12], where N is the number of pixels. This is the main bottleneck. Other steps can be accelerated by FFTs. Table 1 shows that the running time of our method compares

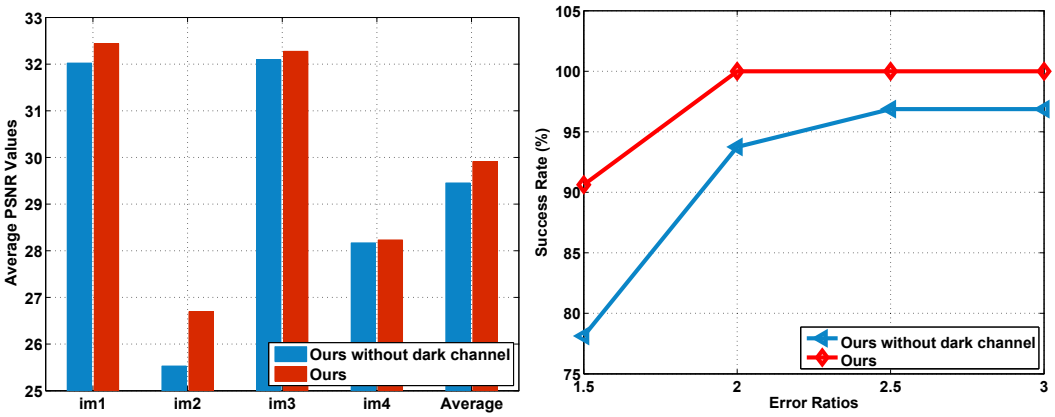

(a) Results on the dataset [10] (b) Results on the dataset [13]

Figure 2. Quantitative results of our method with and without the dark channel prior on two benchmark datasets. The dark channel prior consistently improves the results. In particular, our method with the dark channel prior has 100 % success at error ratio 2 on the dataset by Levin *et al*. [13].

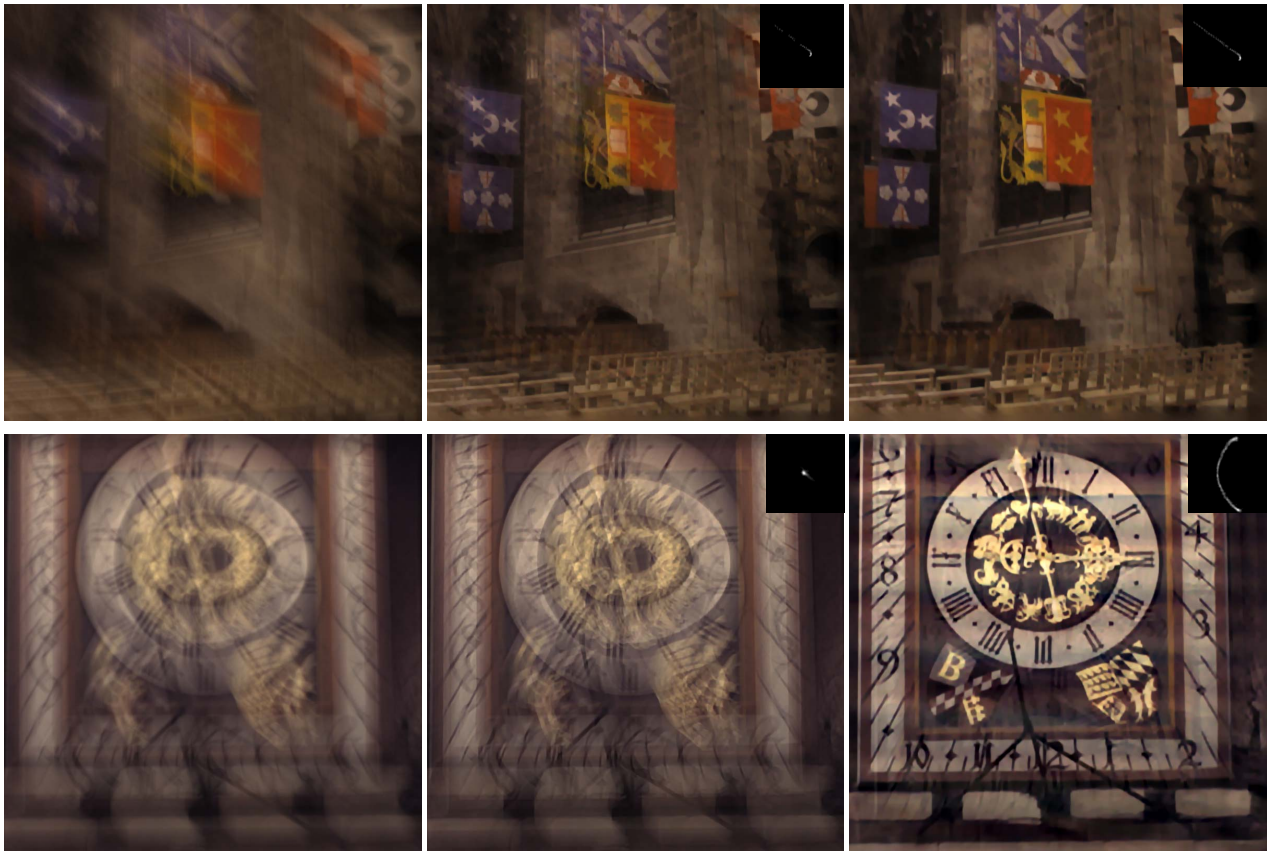

(a) Blurred images (b) Ours without using dark channel prior (c) Ours using dark channel prior

Figure 3. Effectiveness of the proposed dark channel prior in natural image deblurring. Both theoretical and empirical analysis shows that the dark channel prior favors clear image over blurred image. The deblurring method without using the proposed dark channel prior is less effective, while the deblurring method with dark channel prior generates clearer images.

favorably against the competing methods and using the dark channel prior moderately increases the running time.

(a) Blurred image (b) Ours without using dark channel prior (c) Ours using dark channel prior

Figure 4. Effectiveness of the proposed dark channel prior in natural image deblurring. Both theoretical and empirical analysis shows that the dark channel prior favors clear image over blurred image. The deblurring method without using the proposed dark channel prior is less effective, while the deblurring method with dark channel prior generates clearer images.

(a) Blurred images (b) Ours without using dark channel prior (c) Ours using dark channel prior

Figure 5. Effectiveness of the proposed dark channel prior in text image deblurring. Both theoretical and empirical analysis shows that the dark channel prior favors clear image over blurred image. The deblurring method without using the proposed dark channel prior is less effective, while the deblurring method with dark channel prior generates much clearer images.

(a) Blurred images (b) Ours without using dark channel prior (c) Ours using dark channel prior

Figure 6. Effectiveness of the proposed dark channel prior in low-illumination image deblurring. Both theoretical and empirical analysis shows that the dark channel prior favors clear image over blurred image. The deblurring method without using the proposed dark channel prior is less effective, while the deblurring method with dark channel prior generates clearer images. The final latent images are generated with the non-blind deblurring method [19].

(a) Blurred images (b) Ours without using dark channel prior (c) Ours using dark channel prior

Figure 7. Effectiveness of the dark channel prior in face image deblurring. Both theoretical and empirical analysis shows that the dark channel prior favors clear image over blurred image. The deblurring method without using the proposed dark channel prior is less effective, while the deblurring method with dark channel prior generates much clearer images.

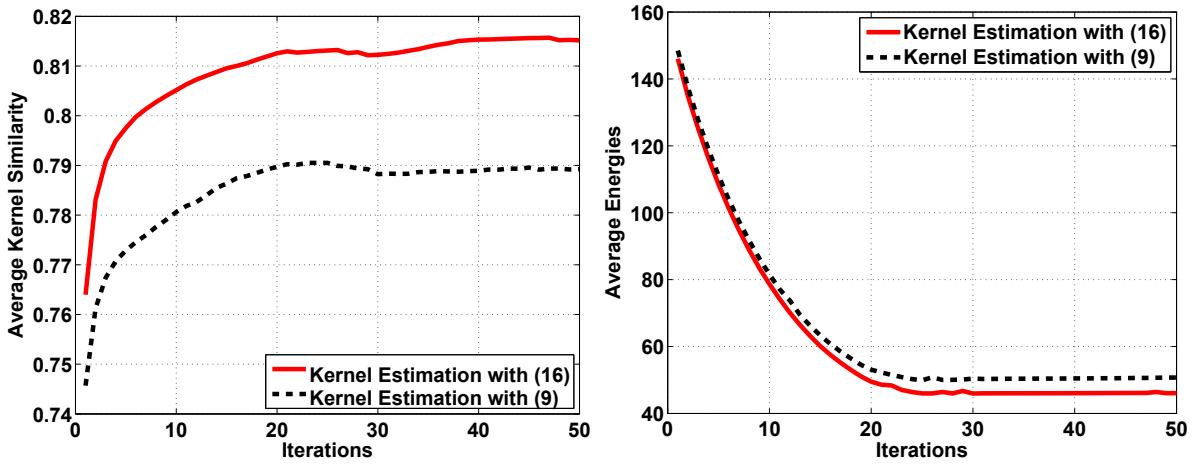

(a) Kernel similarity (b) Objective function value

Figure 8. Fast convergence property of our method, which empirically validates our approximation of the non-linear operator. Note that the kernel estimation methods based on image intensity (i.e., (9) in the manuscript) and gradients (i.e., (16) in the manuscript) have similar convergence property. However, the kernel estimates generated by image gradients have higher kernel similarity values and lower energy values.

4.3. Effect of the Patch Size for computing $D(I)$

Computing the dark channel requires specifying the patch size. Here we discuss the effect of this parameter. We conduct experiments on the dataset [13] with different patch sizes and use PSNR metric to evaluate the quality of restored images, as shown in Table 2. Empirically, we find that our method is robust to the patch size. Note that the image resolution in [13] is 255×255 and we only test the maximum patch size 45 in this dataset. It is an interesting question worth further investigation how the patch size and the image resolution affect the accuracy.

4.4. Limitations of the Proposed Method

Our method assumes that the latent image contains dark (zero-intensity) pixels (**Property 2** in the manuscript). If an image does not contain dark pixels, the dark channel prior has little effect in the image deblurring process. Figure 9 shows

Table 1. Running time (/s) comparisons (obtained on the same PC). "Ours with naive implementation" denotes that $D(I)$ and $\mathbf{M}$ are computed by naive implementations. Computing $D(I)$ and $\mathbf{M}$ according to [12] is able to reduce the running time.

Method	255×255	600×600	800×800
Xu *et al*. [33] (C++)	1.11	3.56	4.31
Krishnan *et al*. [16] (Matlab)	24.23	111.09	226.58
Levin *et al*. [18] (Matlab)	117.06	481.48	917.84
Ours without $D(I)$ (Matlab)	2.77	15.65	28.94
Ours with naive implementation (Matlab)	134.31	691.71	964.90
Ours (Matlab)	17.07	115.86	195.80

Table 2. Quantitative evaluation of patch size on the dataset [13]. Empirically our method is robust to the patch size.

Patch size	15×15	25×25	35×35	45×45
Average PSNRs	30.79	30.95	31.08	30.92

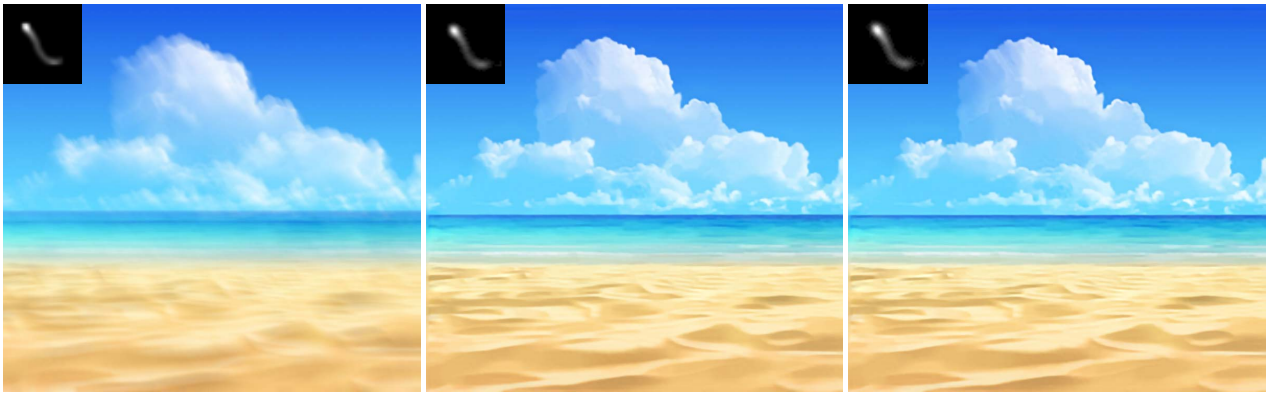

(a) Blurred image and blur kernel (b) Ours without using dark channel prior (c) Ours using dark channel prior

(a) Dark channel of clear image (b) Dark channel of blurred image (c) Our estimated dark channel

Figure 9. One limitation of our method. The dark channel of clear image does not contain zero-elements, which does not hold for our assumption in **Property 2**. For such cases, we always have $\|D(B)\|_0 = \|D(I)\|_0$. The dark channel prior does not help kernel estimation and deblurring results generated with and without dark channel prior are almost the same.

an example where the latent image does not contain dark pixel. The results generated with and without dark channel prior are almost the same. Our method fails gracefully when the dark channel of the original image is not sparse. Noise may cause problem to our method. Noise changes the minimum intensity value of an image patch, while our method assumes that the change to the minimum intensity value is purely due to the blur process. As a result our method is less effective for blurred images with large noise. Figure 10 shows an example which contains Gaussian noise. Our method without using dark channel prior generates much clearer deblurred image. In contrast, the deblurred image generated using dark channel prior still contains blur effect, which indicates that the dark channel prior is not robust to the image noise.

We also evaluate our method using blurred images with Salt & Pepper noise. Figure 11 shows a noisy example from [2].

(a) Blurred image

(b) Ours without using dark channel prior

(c) Ours using dark channel prior

(d) Ours with Gaussian filter

Figure 10. The proposed dark channel prior is sensitive to the Gaussian noise. Since the noise will change the minimum intensity value of an image patch, the deblurred image generated with dark channel prior still contains blur effect as shown in the parts in red boxes in (c), while the deblurred image generated without using dark channel prior is much clearer. We note that although the kernel estimate looks better after applying Gaussian filter to the blurred input, the final deblurred image looks over smooth and still contains ringing artifacts as shown in the red box in (d) due to influence of the filter.

Since the intensity values of this kind of noise are large, our method with and without using dark channel prior both fail to generate clear images. However, we can first use Gaussian filter to the blurred input and then apply our deblurring algorithm to reduce the influence of noise. The results in Figure 11(d) demonstrate that the performance of kernel estimate is greatly improved which accordingly leads to a much clearer deblurred image. Future work will consider joint deblurring and denoising with the dark channel prior in a principled way.

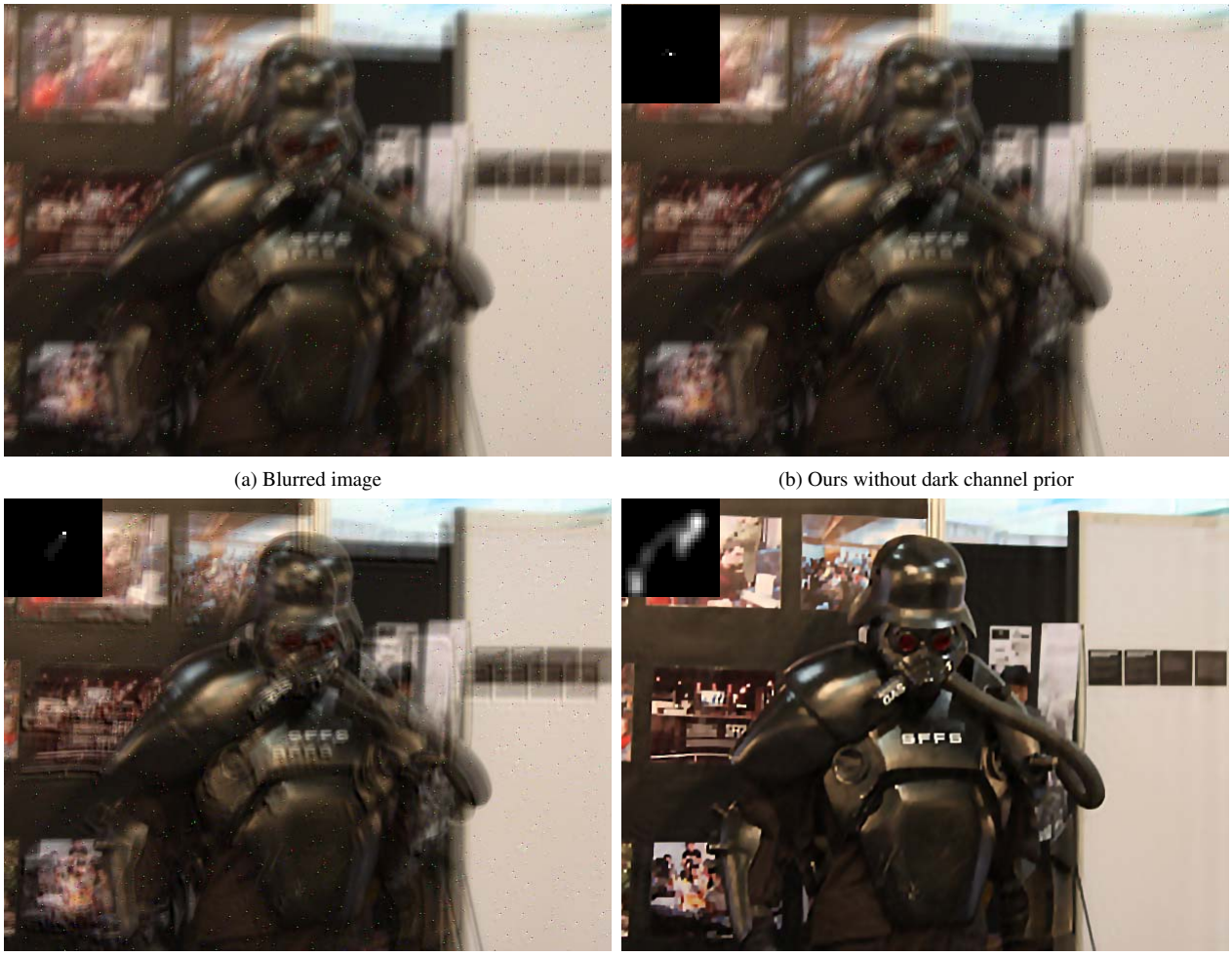

(a) Blurred image

(b) Ours without dark channel prior

(c) Ours with dark channel prior

(d) Ours with Gaussian filter

Figure 11. The proposed dark channel prior is sensitive to the Salt & Pepper noise. Since the intensity values of this kind of noise are large, it will change the minimum intensity value of an image patch. The estimated blur kernel looks like a delta kernel due to influence of noise. One solution to reduce the influence of noise is that we can first apply the Gaussian filter to the blurred images and then use our method to estimate blur kernels. The performance of kernel estimation result is greatly improved as shown in (d). The final deblurring results are generated by the non-blind deblurring method [2].

Algorithm 1 Algorithm for Solving (10)

Input: Blurred image B and blur kernel k.
$I \leftarrow B$, $\beta \leftarrow \beta_0$.
repeat
  solve for $D(I)$ according to the definition of dark channel.
  solve for u using (6).
  $\alpha \leftarrow \alpha_0$.
  repeat
    solve for g using (7).
    solve for I using (9).
    $\alpha \leftarrow 2\alpha$.
  until $\alpha > \alpha_{\max}$
  $\beta \leftarrow 2\beta$.
until $\beta > \beta_{\max}$
Output: Intermediate latent image I.

5. Algorithm for Solving the Latent Image (10)

The objective function for estimating the latent image, *i.e.* (10) in the manuscript, is

$$\min_{I,u,g} \|I \otimes k - B\|_2^2 + \alpha\|\nabla I - g\|_2^2 + \beta\|D(I) - u\|_2^2 + \mu\|g\|_0 + \lambda\|u\|_0. \tag{5}$$

Our optimization is based on the half-quadratic splitting L_0 minimization approach [22] and look-up table method. In the manuscript, we give the closed-form solution of u, *i.e.*,

$$u = \begin{cases} D(I), & |D(I)|^2 \geqslant \frac{\lambda}{\beta}, \\ 0, & \text{otherwise}, \end{cases} \tag{6}$$

Similar to (6), the solution of g is

$$g = \begin{cases} \nabla I, & |\nabla I|^2 \geqslant \frac{\mu}{\alpha}, \\ 0, & \text{otherwise}. \end{cases} \tag{7}$$

Since the problem (13) in the manuscript is a least squares problem, we can get its solution by solving the linear equation,

$$(\mathbf{T}_k^\top \mathbf{T}_k + \beta \mathbf{M}^\top \mathbf{M} + \alpha(\nabla_h^\top \nabla_h + \nabla_v^\top \nabla_v))\mathbf{I} = \mathbf{T}_k^\top \mathbf{B} + \beta \mathbf{M}^\top \mathbf{u} + \alpha(\nabla_h^\top \mathbf{g}_h + \nabla_v^\top \mathbf{g}_v), \tag{8}$$

where ∇_h and ∇_v denote the matrices of the horizontal and vertical differential operators. As (8) involves large matrices, we apply fast Fourier transforms (FFT) to solve it. Note that the matrix $\mathbf{M}$ maps an image to its dark channel and thus the transpose of $\mathbf{M}$ is its inverse operator. The matrix $\mathbf{M}$ is determined by the index between an image and its corresponding dark channel. We record the index when computing the dark channel of an image and use this index to map the solution of u to an image $\widetilde{u}$. Based on this look-up-table-based method, we can obtain the solution of I by

$$\mathbf{I} = \mathcal{F}^{-1}\left(\frac{\overline{\mathcal{F}(\mathbf{T}_k)}\mathcal{F}(\mathbf{B}) + \beta\mathcal{F}(\widetilde{\mathbf{u}}) + \alpha(\overline{\mathcal{F}(\nabla_h)}\mathcal{F}(\mathbf{g}_h) + \overline{\mathcal{F}(\nabla_v)}\mathcal{F}(\mathbf{g}_v))}{\overline{\mathcal{F}(\mathbf{T}_k)}\mathcal{F}(\mathbf{T}_k) + \beta + \alpha(\overline{\mathcal{F}(\nabla_h)}\mathcal{F}(\nabla_h) + \overline{\mathcal{F}(\nabla_v)}\mathcal{F}(\nabla_v))}\right), \tag{9}$$

where $\mathcal{F}(\cdot)$ and $\mathcal{F}^{-1}(\cdot)$ denote the Fourier transform and its inverse transform, respectively; the $\overline{\mathcal{F}(\cdot)}$ is the complex conjugate operator; $\widetilde{\mathbf{u}}$ is the vector form of $\widetilde{u}$. The main steps for solving (10) are summarized in Algorithm 1.

6. Non-Uniform Deblurring Algorithm

As mentioned in the manuscript, our non-uniform deblurring process is carried out by alternatively solving

$$\min_{\mathbf{I}} \|\mathbf{K}\mathbf{I} - \mathbf{B}\|_2^2 + \lambda\|\mathbf{D}(\mathbf{I})\|_0 + \mu\|\nabla\mathbf{I}\|_0 \tag{10}$$

and

$$\min_{\mathbf{k}} \|\mathbf{A}\mathbf{k} - \mathbf{B}\|_2^2 + \gamma\|\mathbf{k}\|_2^2. \tag{11}$$

Estimating Latent Image: For (10), we follow the solver of (8) in the manuscript and rewrite it as

$$\min_{\mathbf{I},\mathbf{u},\mathbf{g}} \|\mathbf{K}\mathbf{I}-\mathbf{B}\|_2^2+\alpha\|\nabla\mathbf{I}-\mathbf{g}\|_2^2+\beta\|\mathbf{D}(\mathbf{I})-\mathbf{u}\|_2^2+\mu\|\mathbf{g}\|_0+\lambda\|\mathbf{u}\|_0, \tag{12}$$

where $\mathbf{u}$ and $\mathbf{g}$ are vector forms of u and g defined in (5). The solutions with respect to $\mathbf{u}$ and $\mathbf{g}$ are still the same to (6) and (7). For the subproblem with respect to $\mathbf{I}$, *i.e.*,

$$\min_{\mathbf{I}} \|\mathbf{K}\mathbf{I}-\mathbf{B}\|_2^2+\alpha\|\nabla\mathbf{I}-\mathbf{g}\|_2^2+\beta\|\mathbf{D}(\mathbf{I})-\mathbf{u}\|_2^2. \tag{13}$$

we use forward approximation with locally-uniform assumption presented in [8] to solve it. Based on [8], we divide the blurred image into $\mathcal{P}$ patches and make two adjacent patches have 50% overlap area. Thus, we can rewrite $\mathbf{B}=\mathbf{K}\mathbf{I}$ as

$$B=\sum_{p=1}^{\mathcal{P}} a_p \otimes (m_p \odot I), \tag{14}$$

where a_p is the blur kernel for the p-th patch, $\odot$ is an element-wise product operator, and m_p is a window function and has the same size as I, which satisfies

$$\sum_{p=1}^{\mathcal{P}} m_p = 1. \tag{15}$$

According to [8], the blur kernel a_r in the p-th patch can be expressed as

$$a_p=\sum_t k_t b_t^p, \tag{16}$$

where t is the index of camera pose samples and b_t^p is the kernel basis in the p-th patch, which can be computed in advance based on the homography matrix [20].

Based on (14), we can model the non-uniform blur process as

$$\mathbf{B}\approx \mathbf{Z}_{\mathbf{I}}^{-1}\sum_{p=1}^{\mathcal{P}} \mathcal{C}_p^{-1}(\mathcal{F}^{-1}(\mathrm{diag}(\mathcal{F}(\mathbf{Z}_a a_p)))\mathcal{F}(\mathcal{C}_p \mathrm{diag}(m_p)))\mathbf{I}, \tag{17}$$

where $\mathcal{C}_p(\cdot)$ is an operator that chops the p-th patch from an image, $\mathcal{C}_p^{-1}(\cdot)$ is the operator to paste the patch back to the image, $\mathbf{Z}_{\mathbf{I}}$ and $\mathbf{Z}_a$ are the zero-padding matrix that prepend zeros to a vector such that its size matches the size of the vector resulting from the summation, $\mathrm{diag}(x)$ is a diagonal matrix with the element of vector x on the main diagonal.

Based on (17), the solution of (13) is

$$\mathbf{I}=\frac{1}{W}\sum_{p=1}^{\mathcal{P}}\mathcal{C}_p^{-1}\left(\mathcal{F}^{-1}\left(\frac{\overline{\mathcal{F}(\mathbf{Z}_a a_p)}\mathcal{F}(\mathcal{C}_p\mathrm{diag}(m_p)\mathbf{B})+\beta\mathcal{F}(\mathcal{C}_p(\tilde{\mathbf{u}}))+\alpha(\overline{\mathcal{F}(\mathcal{C}_p(\nabla_h))}\mathcal{F}(\mathcal{C}_p(g_h))+\overline{\mathcal{F}(\mathcal{C}_p(\nabla_v))}\mathcal{F}(\mathcal{C}_p(g_v)))}{\overline{\mathcal{F}(\mathbf{Z}_a a_p)}\mathcal{F}(\mathbf{Z}_a a_p)+\beta+\alpha(\overline{\mathcal{F}(\mathcal{C}_p(\nabla_h))}\mathcal{F}(\mathcal{C}_p(\nabla_h))+\overline{\mathcal{F}(\mathcal{C}_p(\nabla_v))}\mathcal{F}(\mathcal{C}_p(\nabla_v)))}\right)\right), \tag{18}$$

where W is a weight to suppress visual artifacts caused by the window functions [8]. The algorithm for solving (10) is similar to Algorithm 1, where we only need to replace (9) with (18).

Estimating Blur Kernel: As to the kernel estimation model (11), we use the same optimization method proposed by [23]. The main steps of non-uniform algorithm are same as Algorithm 1 in the manuscript.

7. Quantitative Evaluations on the Available Deblurring Datasets

To verify the effectiveness of our method, we evaluate it on the publicly available deblurring datasets [10, 13, 18]. The results are shown in Figure 12.

8. More Experimental Results

In this section, we provide more visual comparisons with state-of-the-art deblurring methods.

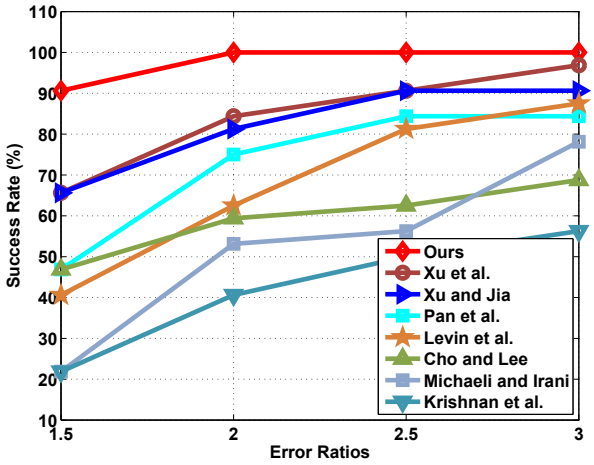

(a) Quantitative evaluations on dataset [13]

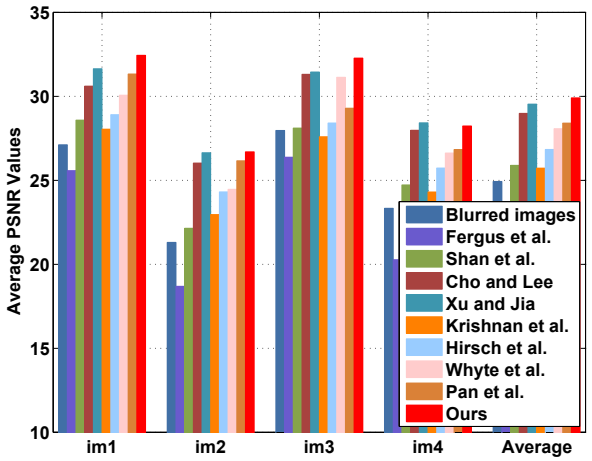

(b) Quantitative evaluations on dataset [10]

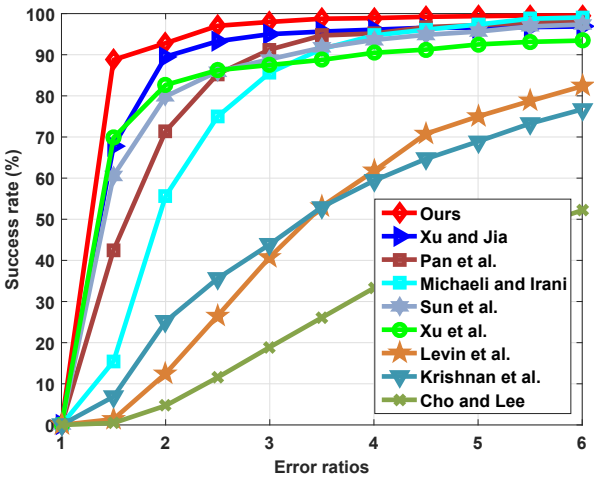

(c) Quantitative evaluations on dataset [18]

Figure 12. Quantitative evaluations on the publicly available deblurring datasets [13, 10, 18]. The dataset by Levin *et al*. [13] contains 32 blurred examples including 4 clear images and 8 blur kernels. The dataset by Köhler *et al*. [10] contains 48 blurred examples, including 4 clear images and 12 challenging blur kernels. The dataset by Sun *et al*. [18] contains 640 blurred examples, which includes 80 clear images and 8 blur kernels from [13]. Our method performs competitively with state-of-the-art methods. In particular, our method is the only one that has 100 % success at error ratio 2 on dataset [13].

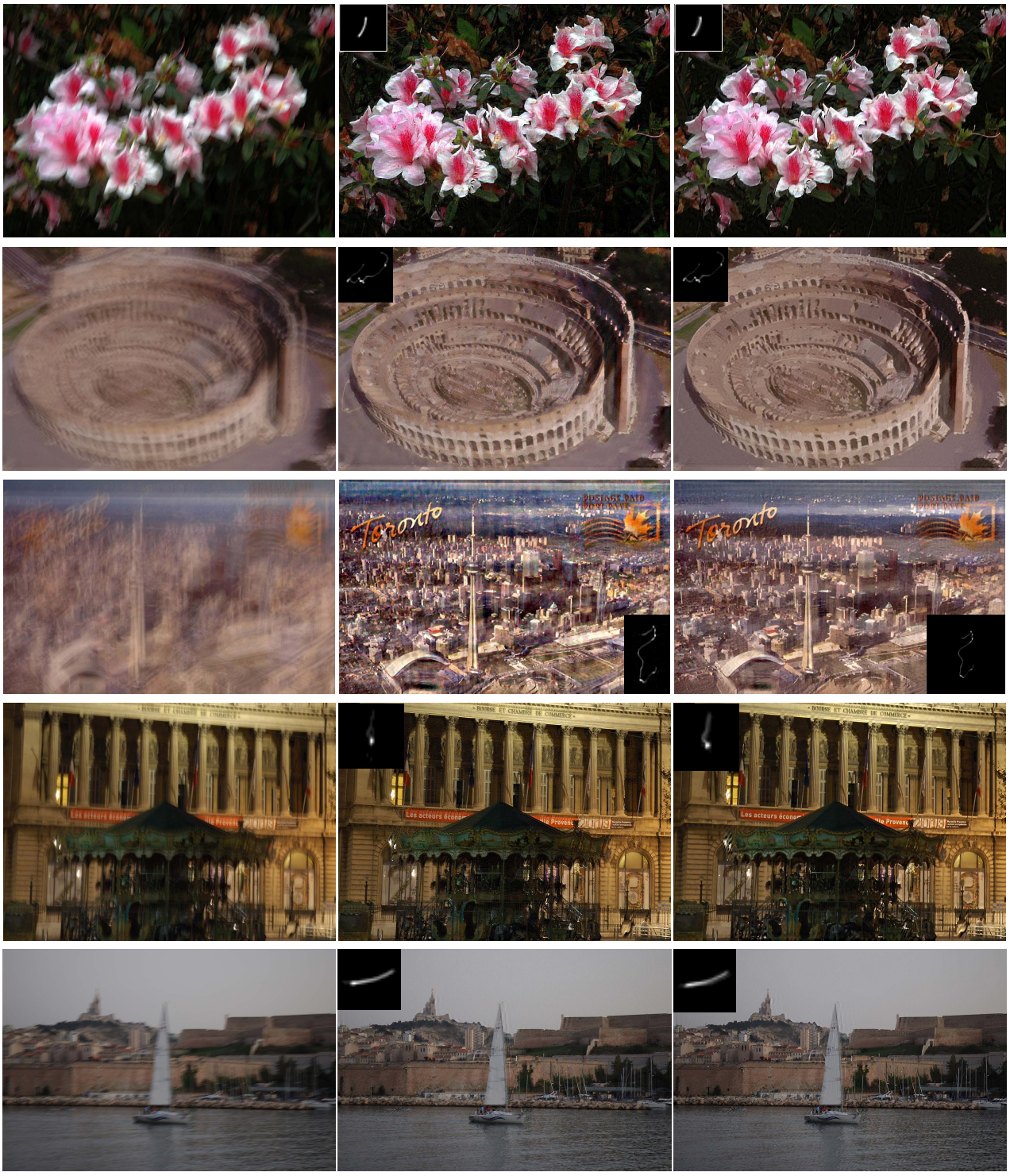

(a) Blurred image (b) Xu and Jia [21] (c) Ours

Figure 13. Natural image deblurring examples from [21]. Our method generates visually comparable or even better deblurring results compared to the reported results in [21].

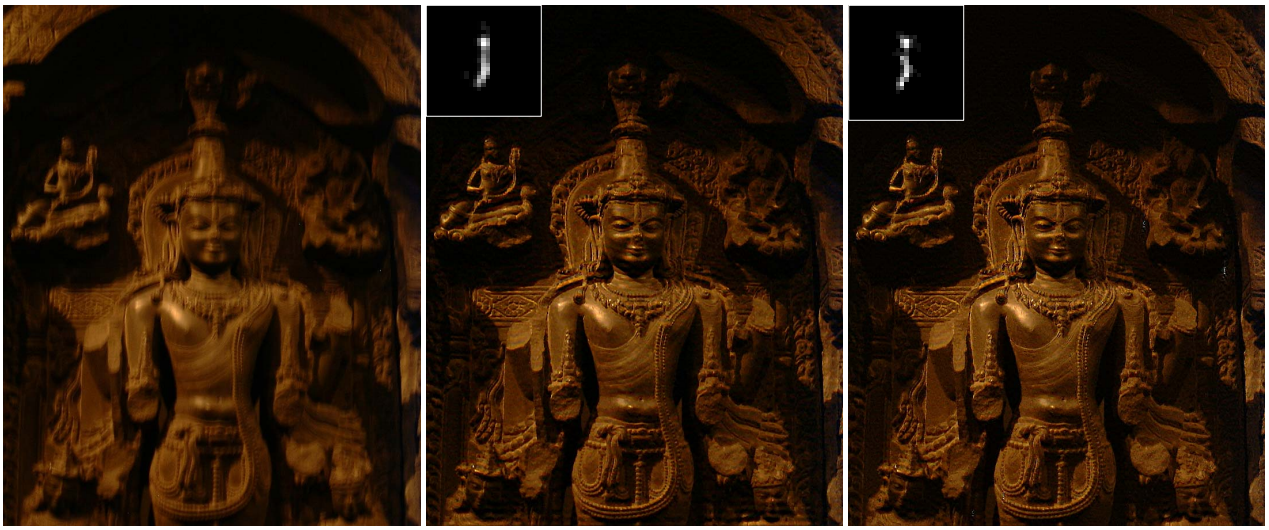

(a) Blurred image (b) Xu and Jia [21] (c) Ours

(a) Blurred image (b) Xu and Jia [21] (c) Ours

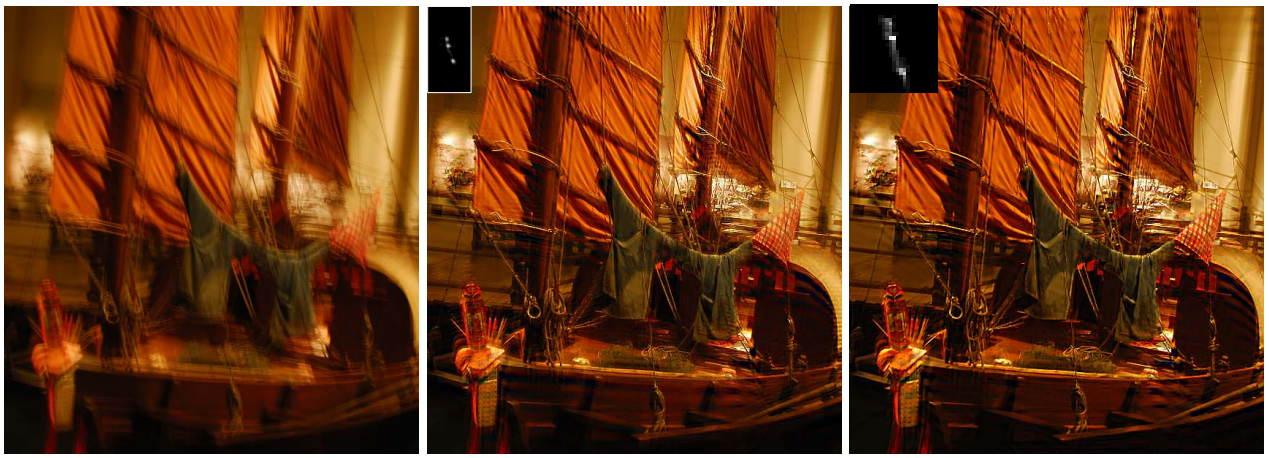

(a) Blurred image (b) Xu *et al*. [23] (c) Ours

Figure 14. Comparisons with state-of-the-art deblurring methods using their provided examples and reported results. Our method generates visually comparable or even better deblurring results.

(a) Blurred image (b) Fergus *et al*. [4] (c) Ours

(a) Blurred image (b) Shan *et al*. [17] (c) Ours

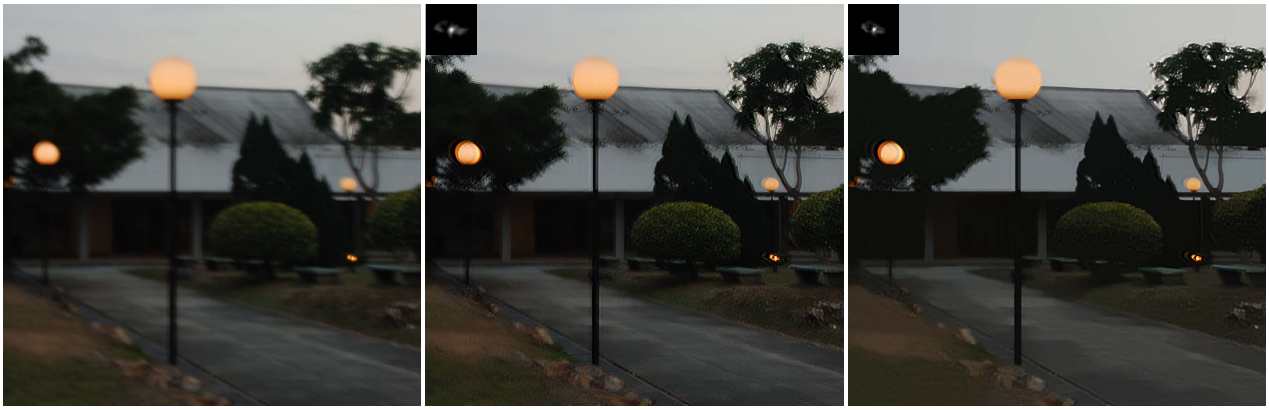

(a) Blurred image (b) Shan *et al*. [17] (c) Ours

(a) Blurred image (b) Cho and Lee [1] (c) Ours

Figure 15. Comparisons with state-of-the-art deblurring methods using their provided examples and reported results. Our method generates visually comparable or even better deblurring results.

(a) Blurred image (b) Cho and Lee [1] (c) Ours

(a) Blurred image (b) Cho and Lee [1] (c) Ours

(a) Blurred image (b) Krishnan *et al*. [11] (c) Ours

Figure 16. Comparisons with state-of-the-art deblurring methods using their provided examples and reported results. Our method generates visually comparable or even better deblurring results.

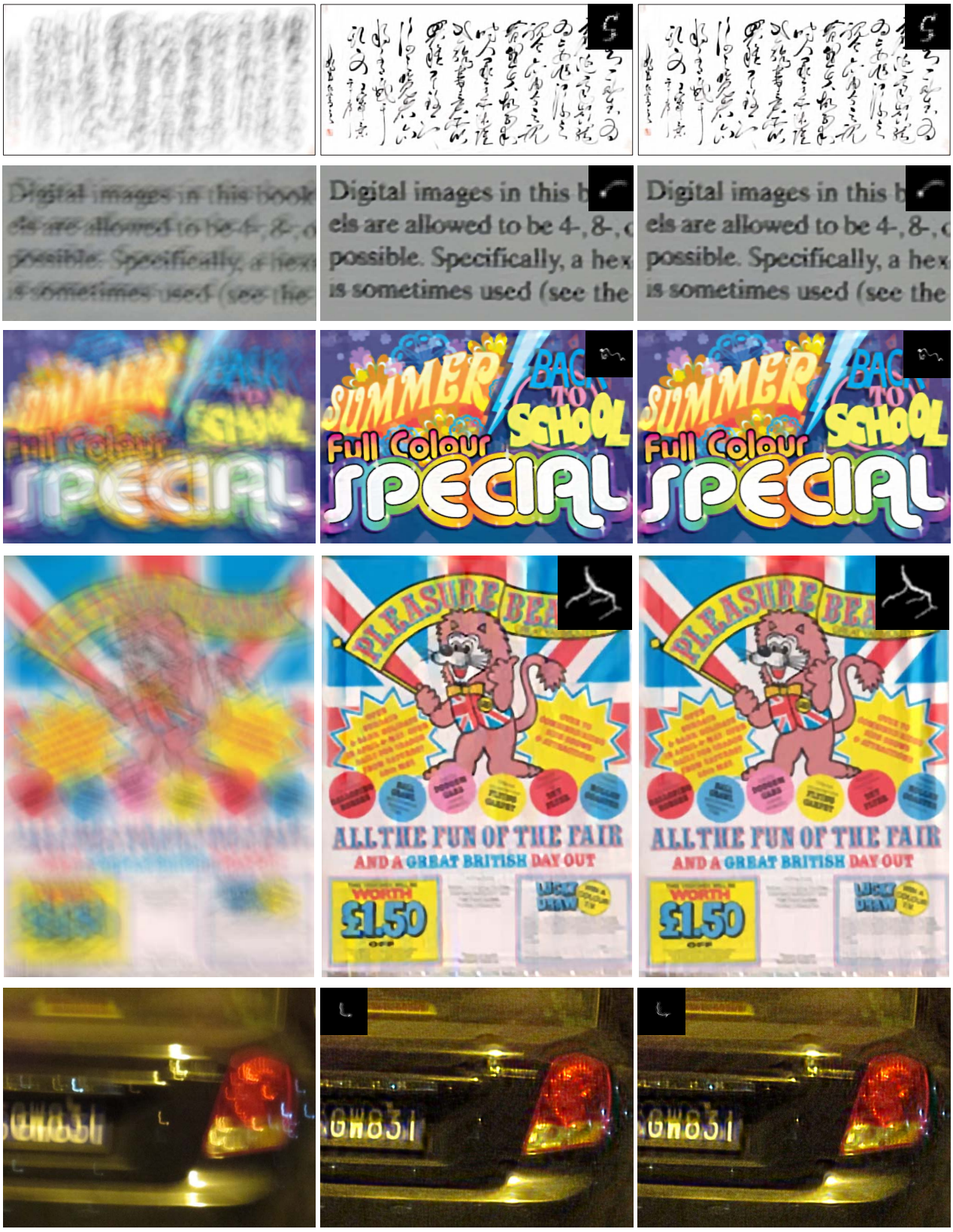

(a) Blurred image (b) Pan *et al*. [15] (c) Ours

Figure 17. Comparisons with state-of-the-art text deblurring method [15]. Our method generates visually comparable or even better deblurring results than the reported results in [15].

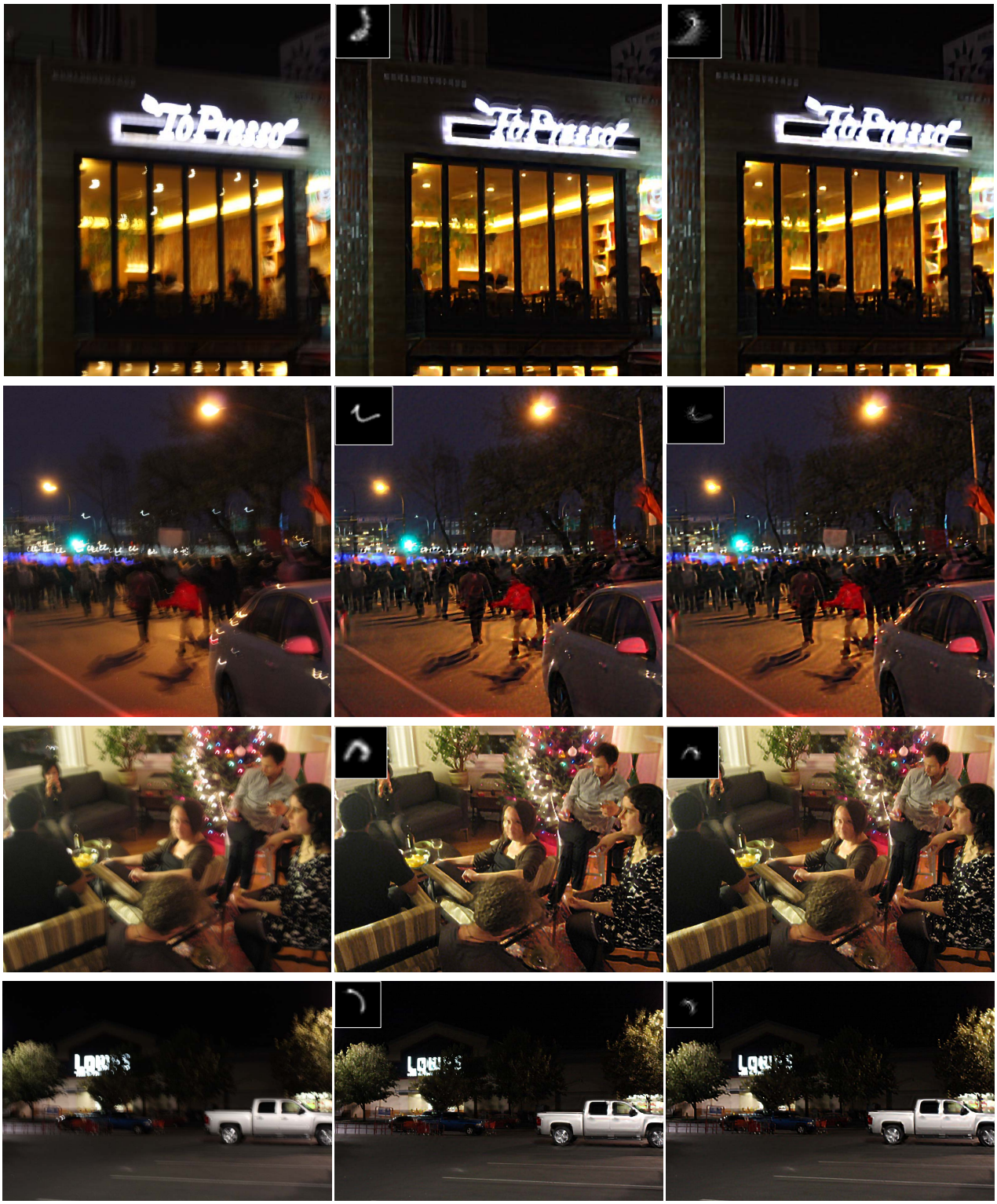

(a) Blurred image (b) Hu *et al*. [9] (c) Ours

Figure 18. Comparisons with state-of-the-art low-light image deblurring method [9]. The final deblurring results are generated by the non-blind deblurring method [9] for fair comparisons. Our method generates visually comparable or even better deblurring results than the reported results in [9].

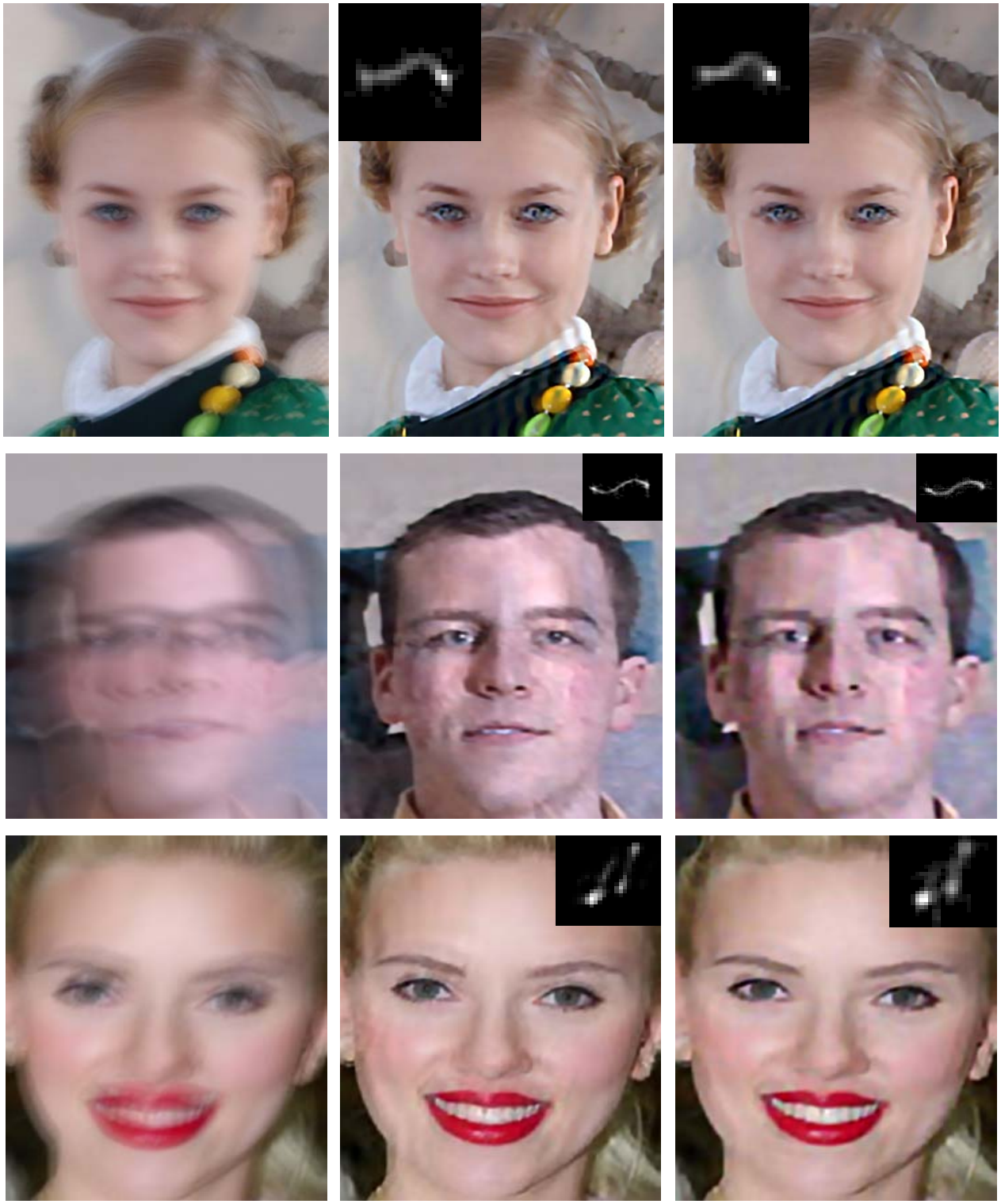

(a) Blurred image (b) Pan *et al*. [14] (c) Ours

Figure 19. Comparisons with state-of-the-art face image deblurring method [14]. The final deblurring results are generated with the same non-blind deblurring method used in [14] for fair comparisons. Our method generates visually comparable or even better deblurring results than the reported results in [14].

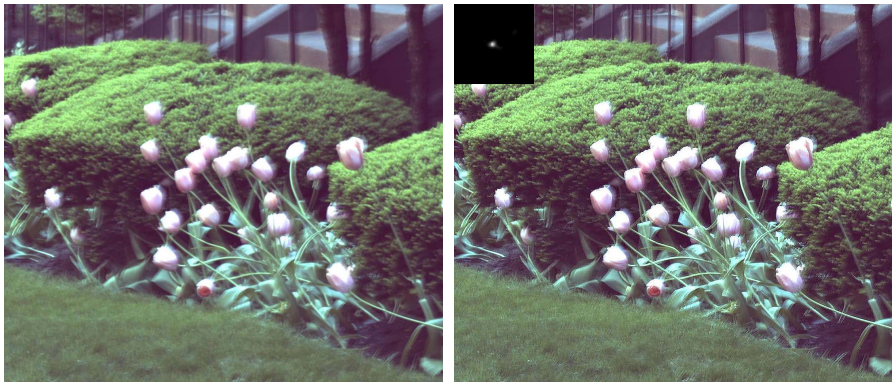

(a) Blurred image

(b) Cho and Lee [1]

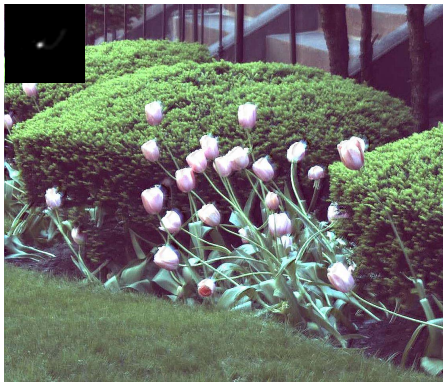

(c) Xu and Jia [21]

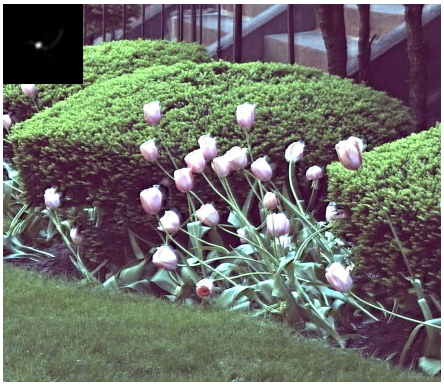

(d) Krishnan *et al*. [11]

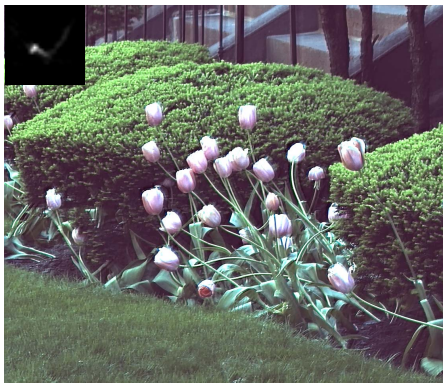

(e) Goldstein and Fattal [5]

(f) Cho *et al*. [3]

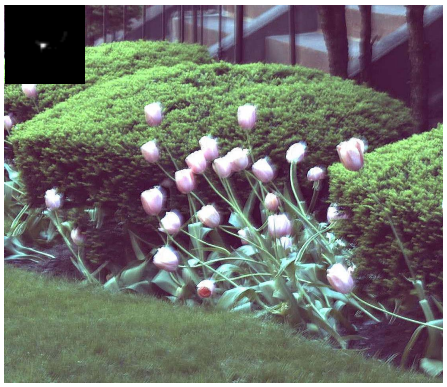

(g) Xu *et al*. [23]

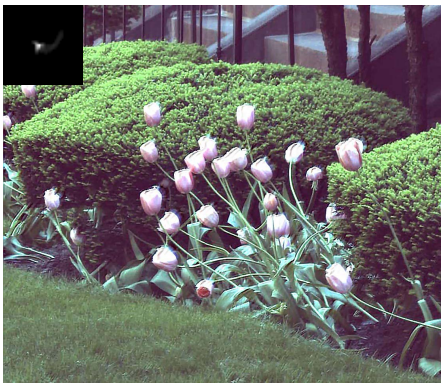

(h) Ours

Figure 20. Comparisons with state-of-the-art deblurring methods using real examples. Our method generates clear deblurred images.

(a) Blurred image (b) Cho and Lee [1]

(c) Xu and Jia [21] (d) Krishnan *et al*. [11]

(e) Levin *et al*. [13] (f) Zhong *et al*. [24]

(g) Xu *et al*. [23] (h) Ours

Figure 21. Comparisons with state-of-the-art deblurring methods using real examples. As this image contains several saturated areas, we use the non-blind deblurring method [2] to generate the final deblurring results for fair comparisons. The parts in black boxes contain some fake structures. Our method generates visually comparable or even better deblurring results.

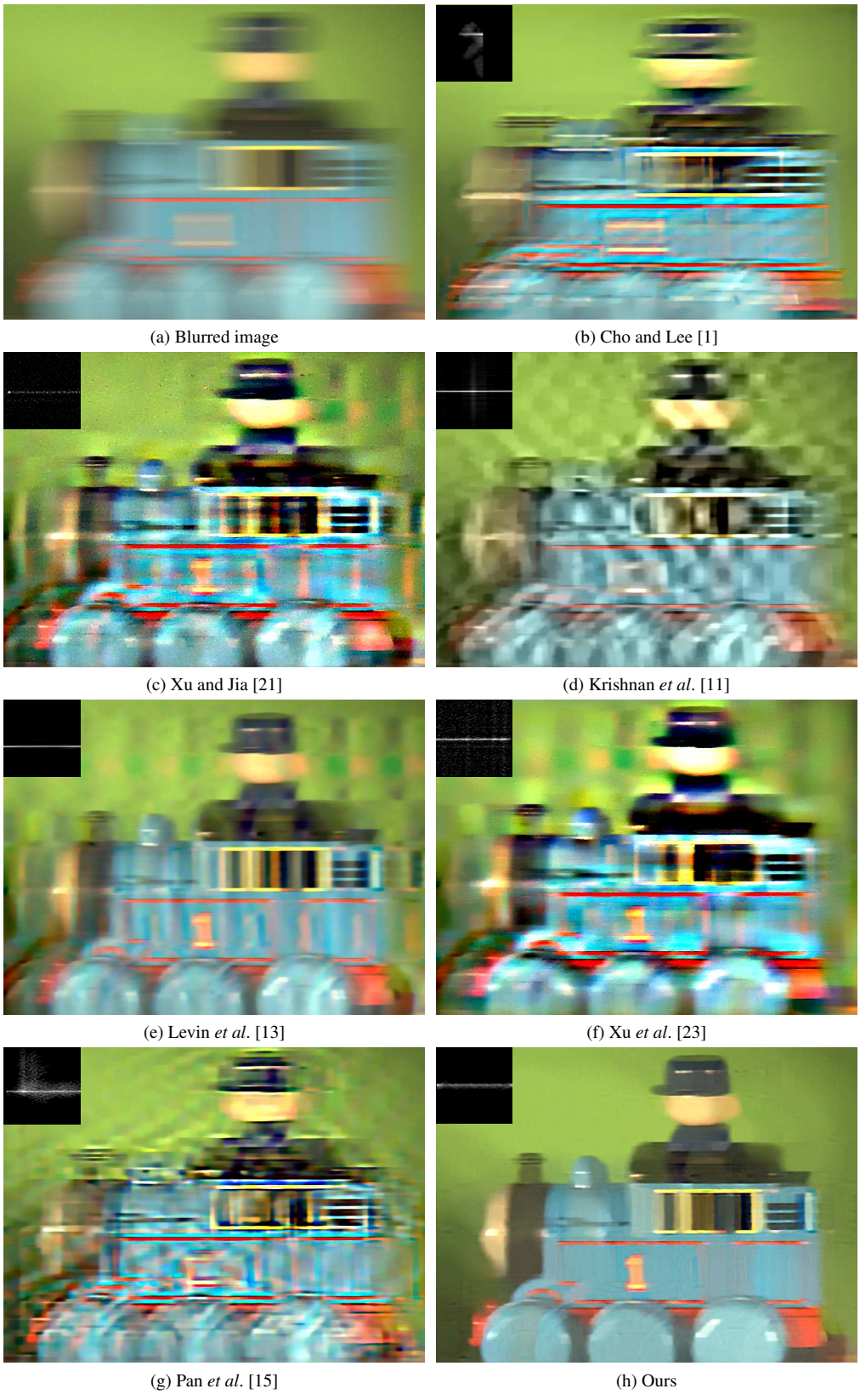

(a) Blurred image

(b) Cho and Lee [1]

(c) Xu and Jia [21]

(d) Krishnan *et al*. [11]

(e) Levin *et al*. [13]

(f) Xu *et al*. [23]

(g) Pan *et al*. [15]

(h) Ours

Figure 22. An example from [16]. Our method generates a clear deblurred image.

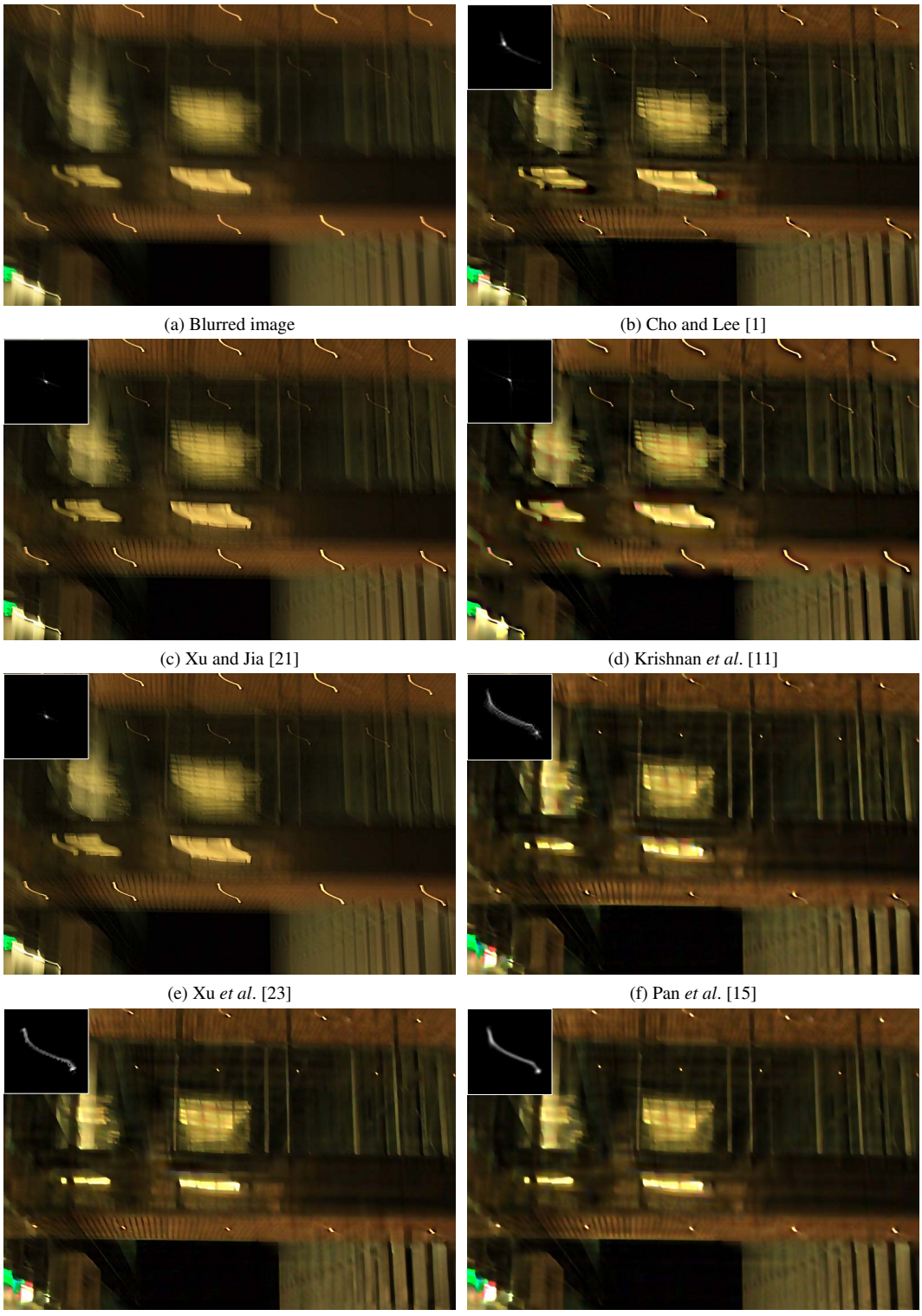

(a) Blurred image (b) Cho and Lee [1]

(c) Xu and Jia [21] (d) Krishnan *et al*. [11]

(e) Xu *et al*. [23] (f) Pan *et al*. [15]

(g) Hu *et al*. [9] (h) Ours

Figure 23. A real captured image with several low-light streaks and saturated areas. The state-of-the-art natural image deblurring methods [1, 21, 11, 23] fail to estimate blur kernels due to the influence of saturated areas. Although the text deblurring method [15] is able to estimate blur kernels, the final deblurred image still contain blur effect. Compared to the low-light image deblurring method [9], our method generates comparable results both in the latent image and kernel. The final deblurring results are generated by the non-blind deblurring method [9] for fair comparisons.

(a) Blurred image (b) Cho and Lee [1]

(c) Xu and Jia [21] (d) Krishnan *et al*. [11]

(e) Zhong *et al*. [24] (f) Xu *et al*. [23]

(g) Pan *et al*. [15] (h) Ours

Figure 24. A real captured image. The state-of-the-art natural image deblurring methods [1, 21, 11, 24] fail to estimate blur kernels. Compared to the image deblurring methods [23, 15], our method generates a better deblurred image with much clearer characters.

(a) Input

(b) Krishnan *et al*. [11]

(c) Whyte *et al*. [20]

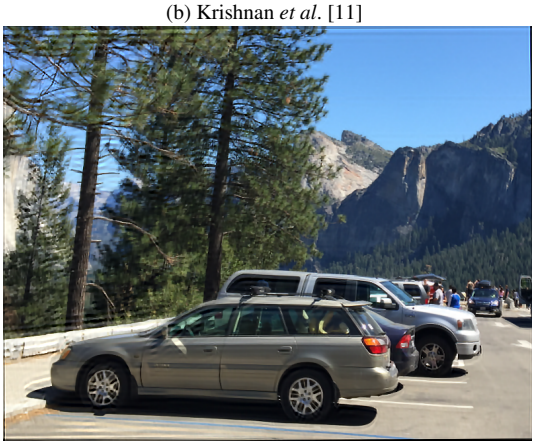

(d) Xu *et al*. [23]

(e) Ours

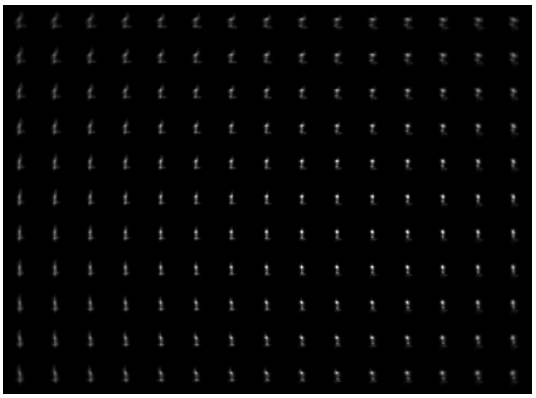

(f) Our kernels

Figure 25. Non-uniform deblurring. Our method generates much clearer images.

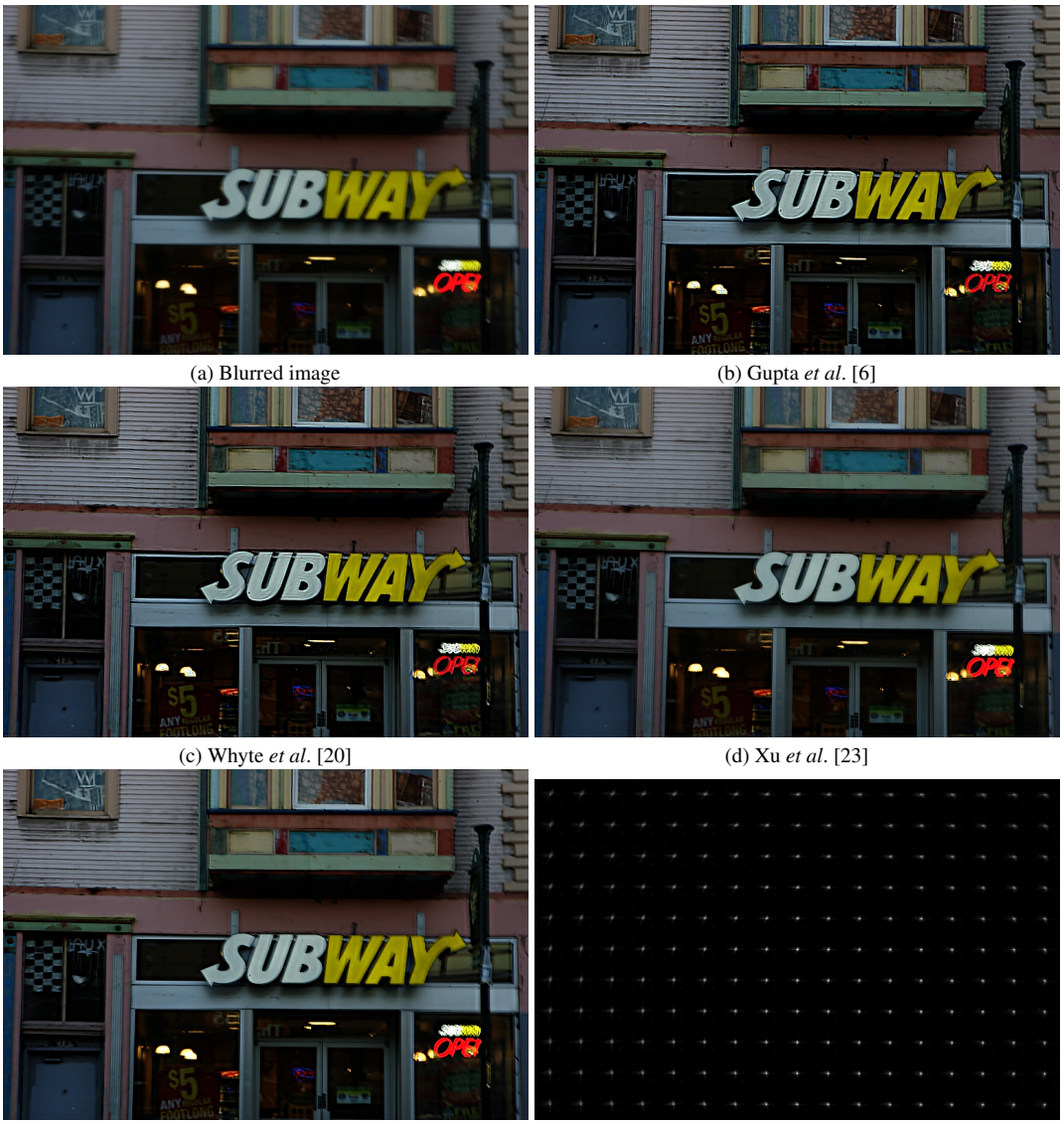

(a) Blurred image (b) Gupta *et al*. [6]

(c) Whyte *et al*. [20] (d) Xu *et al*. [23]

(e) Ours (f) Our estimated kernels

Figure 26. Non-uniform examples from [6]. We use the same non-blind deblurring method used in [23] to recover our final deblurring result. Our method generates comparable results.

(a) Blurred image (b) Gupta *et al*. [6]

(c) Whyte *et al*. [20] (d) Xu *et al*. [23]

(e) Ours (f) Our estimated kernels

Figure 27. Non-uniform examples from [6]. We use the same non-blind deblurring method used in [23] to recover our final deblurring result. Our method generates comparable results.

References

[1] S. Cho and S. Lee. Fast motion deblurring. In *SIGGRAPH Asia*, volume 28, page 145, 2009. 15, 16, 20, 21, 22, 23, 24

[2] S. Cho, J. Wang, and S. Lee. Handling outliers in non-blind image deconvolution. In *ICCV*, pages 495–502, 2011. 7, 9, 21

[3] T. S. Cho, S. Paris, B. K. P. Horn, and W. T. Freeman. Blur kernel estimation using the radon transform. In *CVPR*, pages 241–248, 2011. 20

[4] R. Fergus, B. Singh, A. Hertzmann, S. T. Roweis, and W. T. Freeman. Removing camera shake from a single photograph. *ACM SIGGRAPH*, 25(3):787–794, 2006. 15

[5] A. Goldstein and R. Fattal. Blur-kernel estimation from spectral irregularities. In *ECCV*, pages 622–635, 2012. 20

[6] A. Gupta, N. Joshi, C. L. Zitnick, M. F. Cohen, and B. Curless. Single image deblurring using motion density functions. In *ECCV*, pages 171–184, 2010. 26, 27

[7] K. He, J. Sun, and X. Tang. Single image haze removal using dark channel prior. In *CVPR*, pages 1956–1963, 2009. 2

[8] M. Hirsch, C. J. Schuler, S. Harmeling, and B. Schölkopf. Fast removal of non-uniform camera shake. In *ICCV*, pages 463–470, 2011. 11

[9] Z. Hu, S. Cho, J. Wang, and M.-H. Yang. Deblurring low-light images with light streaks. In *CVPR*, pages 3382–3389, 2014. 3, 18, 23

[10] R. Köhler, M. Hirsch, B. J. Mohler, B. Schölkopf, and S. Harmeling. Recording and playback of camera shake: Benchmarking blind deconvolution with a real-world database. In *ECCV*, pages 27–40, 2012. 1, 2, 4, 11, 12

[11] D. Krishnan, T. Tay, and R. Fergus. Blind deconvolution using a normalized sparsity measure. In *CVPR*, pages 2657–2664, 2011. 2, 3, 16, 20, 21, 22, 23, 24, 25

[12] D. Lemire. Streaming maximum-minimum filter using no more than three comparisons per element. *Nordic Journal of Computing*, 13(4):328–339, 2006. 3, 7

[13] A. Levin, Y. Weiss, F. Durand, and W. T. Freeman. Understanding and evaluating blind deconvolution algorithms. In *CVPR*, pages 1964–1971, 2009. 1, 2, 4, 6, 7, 11, 12, 21, 22

[14] J. Pan, Z. Hu, Z. Su, and M.-H. Yang. Deblurring face images with exemplars. In *ECCV*, pages 47–62, 2014. 19

[15] J. Pan, Z. Hu, Z. Su, and M.-H. Yang. Deblurring text images via L_0-regularized intensity and gradient prior. In *CVPR*, pages 2901–2908, 2014. 3, 17, 22, 23, 24

[16] R. Raskar, A. K. Agrawal, and J. Tumblin. Coded exposure photography: motion deblurring using fluttered shutter. *ACM SIGGRAPH*, 25(3):795–804, 2006. 22

[17] Q. Shan, J. Jia, and A. Agarwala. High-quality motion deblurring from a single image. *ACM SIGGRAPH*, 27(3):73, 2008. 15

[18] L. Sun, S. Cho, J. Wang, and J. Hays. Edge-based blur kernel estimation using patch priors. In *ICCP*, 2013. 1, 11, 12

[19] O. Whyte, J. Sivic, and A. Zisserman. Deblurring shaken and partially saturated images. In *ICCV Workshops*, pages 745–752, 2011. 5

[20] O. Whyte, J. Sivic, A. Zisserman, and J. Ponce. Non-uniform deblurring for shaken images. *IJCV*, 98(2):168–186, 2012. 11, 25, 26, 27

[21] L. Xu and J. Jia. Two-phase kernel estimation for robust motion deblurring. In *ECCV*, pages 157–170, 2010. 13, 14, 20, 21, 22, 23, 24

[22] L. Xu, C. Lu, Y. Xu, and J. Jia. Image smoothing via L_0 gradient minimization. In *SIGGRAPH Asia*, volume 30, page 174, 2011. 10

[23] L. Xu, S. Zheng, and J. Jia. Unnatural L_0 sparse representation for natural image deblurring. In *CVPR*, pages 1107–1114, 2013. 3, 11, 14, 20, 21, 22, 23, 24, 25, 26, 27

[24] L. Zhong, S. Cho, D. Metaxas, S. Paris, and J. Wang. Handling noise in single image deblurring using directional filters. In *CVPR*, pages 612–619, 2013. 21, 24